Applied
Magnetic Resonance

CrossMark

Development of Very-Low-Temperature Millimeter-Wave Electron-Spin-Resonance Measurement System

Y. Fujii[1] · **Y. Ishikawa[2]** · **K. Ohya[1,6]** · **S. Miura[2,7]** · **Y. Koizumi[1]** · **A. Fukuda[3]** · **T. Omija[1]** · **S. Mitsudo[1]** · **T. Mizusaki[1]** · **A. Matsubara[4]** · **H. Yamamori[5]** · **T. Komori[2]** · **K. Morimoto[2,8]** · **H. Kikuchi[2]**

Abstract   We report the development of a millimeter-wave electron-spin-resonance (ESR) measurement system at the University of Fukui using a ^{3}He/^{4}He dilution refrigerator to reach temperatures below 1 K. The system operates in the frequency range of 125–130 GHz, with a homodyne detection. A nuclear-magnetic-resonance (NMR) measurement system was also developed in this system as the extension for millimeter-wave ESR/NMR double magnetic-resonance (DoMR) experiments. Several types of Fabry–Pérot-type resonators (FPR) have been developed: A piezo actuator attached to an FPR enables an electric tuning of cavity frequency. A flat mirror of an FPR has been fabricated using a gold thin film aiming for DoMR. ESR signal was measured down to 0.09 K. Results of ESR measurements of an organic radical crystal and phosphorous-doped silicon are presented. The NMR signal from ^{1}H contained in the resonator is also detected successfully as a test for DoMR.

✉ Y. Fujii
  fujii@apphy.u-fukui.ac.jp

1   Research Center for Development of Far-Infrared Region, University of Fukui, Fukui 910-8507, Japan

2   Department of Applied Physics, Graduate School of Engineering, University of Fukui, Fukui 910-8507, Japan

3   Department of Physics, Hyogo College of Medicine, Mukogawacho 1-1, Nishinomiya, Hyogo 663-8501, Japan

4   Department of Physics, Kyoto University, Kyoto 606-8501, Japan

5   Technical Division, School of Engineering, University of Fukui, Fukui 910-8507, Japan

6   Present Address: KYOCERA Corporation, Kyoto, Japan

7   Present Address: Furukawa Electric Co., Ltd, Tokyo, Japan

8   Present Address: Nidec Corporation, Kyoto, Japan

1 Introduction

Magnetic-resonance techniques such as electron-spin resonance (ESR) [1, 2] and nuclear-magnetic resonance (NMR) [3, 4] are efficient methods for studies of various materials from the microscopic point of view. In particular, ESR can help us to directly investigate the interactions among electrons and between electrons and nuclei of magnetic materials. Phenomena based on the quantum effects of spin systems have been attracting a significant research attention. To study such quantum properties, very low temperatures are often required to suppress thermal fluctuations [5]. Many studies have been reported on NMR and muon spin resonance/relaxation (μSR) measurements in the ultra-low-temperature region below 1 K [6–11]. However, ESR reports at very low temperatures are rather rare [12–22], mainly owing to the technical difficulties such as the heat inflow from the outside through waveguides and cables and heating by electromagnetic waves used to irradiate the sample. Nevertheless, several ESR systems have been cooled to extremely low temperatures using the ^{3}He single-shot method, nuclear adiabatic demagnetization, etc. [12–22]. It is notable that Sakon and coworkers developed an ESR system using a ^{3}He–^{4}He dilution refrigerator (DR), which can be used over a wide-frequency range of 45–110 GHz at temperatures down to 160 mK [18].

When an ESR measurement system is combined with the NMR technique, ESR/NMR double magnetic-resonance (DoMR) techniques could be achieved. The electron nuclear double resonance (ENDOR) [23–26] technique is utilized to provide useful information about electron–nucleus hyperfine interactions. In case that dynamic nuclear polarization (DNP) [27–32] is caused by irradiation of ESR transitions, DNP-NMR is one of the ESR/NMR DoMR techniques. The development of a DNP–NMR system is one of the current central issues in the NMR spectroscopy as well as in medical applications.

A typical example of DNP was reported more than 50 years ago, in an ESR study of a low-phosphorous-doped silicon (Si:P), where a donor electron spin is coupled with a ^{31}P nuclear spin [33]. Since Kane has proposed a magnetic-resonance-type quantum-computer model with Si:P, where the DNP effect is utilized for "initialization" [34], Si:P has been attracting a significant renewed interest. Although the ^{31}P-NMR signal has not been directly observed owing to the low concentration of phosphorus in Si:P, the ^{31}P-NMR detection could be achieved using the DNP. Therefore, Si:P is appropriate as a target sample for a simultaneous ESR and NMR measurement. External magnetic fields above 3 T and ultra-low temperatures below 0.3 K were required for the Kane's quantum-computer demonstration experiments.

Considering the importance of low temperature for studies on quantum effects and quantum information, as well as the recent rapid developments of DoMR techniques, it is highly significant to develop a low-temperature DoMR measurement system. Furthermore, higher magnetic field (and frequency) of the magnetic resonance can improve the resolution of spectrum. Measurement systems that can perform both ESR and NMR at ultra-low temperatures and high magnetic fields are very rare [21, 22].

We have been developing millimeter-wave ESR and DoMR measurement systems for the very-low-temperature range [35–37]. These systems are based on the Fabry–Pérot-type resonator (FPR), composed of two mirrors.

In this paper, we report our recent development of a millimeter-wave homodyne-detection ESR system, using a ^{3}He–^{4}He DR. The NMR system is attached to the ESR system aiming for DoMR. After a brief description of our system in the following section, we describe the developed FPRs: (1) An FPR accommodates a home-made piezo actuator for electric tuning of resonance frequency. (2) A flat mirror of an FPR is made of gold thin film being suitable for DoMR. (3) A coupling iris is placed on a flat mirror to keep the sample at the same position during the tuning of the resonance frequency. Furthermore, we discuss the results of the measurements with the ESR system: ESR results of 1,1-diphenyl-2-picrylhydrazyl (DPPH) radical crystal show that it works as a field marker. ESR spectrum of phosphorous-doped silicon shows DNP effect.

2 Overview of the ESR–NMR System Using a DR

Figure 1 shows a schematic of our millimeter-wave ESR/NMR system with a ^{3}He–^{4}He DR (Kelvinox MX 400, Oxford Instruments plc). The DR unit is installed into a cryostat with an 18-T superconducting magnet (SCM, Oxford Instruments plc).

The ESR system is based on a homodyne-detection system [2, 36–40]. To obtain a better sensitivity of ESR measurements, the InSb detector is anchored at a low temperature of the still stage in the DR. Note that ESR results shown in Sects. 4 and 5.1 were obtained with the detector anchored on the 1-K pot stage. Although the sensitivity for the latter case is a little worse, there is an advantage that the temperature stabilization of the 1-K pot stage is relatively easy even for the case of the sample temperature above ~2 K. This design is achieved using the circulator and isolator, which operate even at very low temperatures, though their frequency band is rather narrow (approximately 125–130 GHz). We used oversized (Q-band) waveguides made of CuNi connected between the room temperature and 4 K to simultaneously achieve a smaller loss and better thermal insulation. D-band CuNi waveguides are also used for the thermal insulation between the stages at different temperatures. At present, we have a loss of 20–24 dB from the tapered waveguide at the entrance to the DR to the end of the waveguide just above the FPR. The lowest temperature at the mixing chamber (M/C) reaches 34 mK [36]. The cooling power at 0.1 K is 240 μW with a still-heater power of 50 mW [36]. We have performed ESR measurements in a temperature range down to 0.09 K, as shown in Sect. 5.1. The lowest temperature depends on the millimeter-wave power.

A phase-locked Gunn diode (PLO-6-128-01, Farran Technology) oscillator has an output power of approximately 10 mW around the central frequency (~128 GHz). The stability of the frequency is approximately 3×10^{-6}. The millimeter-wave source is changed to a backward wave oscillator (BWO, Model OB-76) when a wide sweep of the frequency is necessary to, for example, observe a resonance frequency of FPR changing as the mirror distance of FPR is changed.
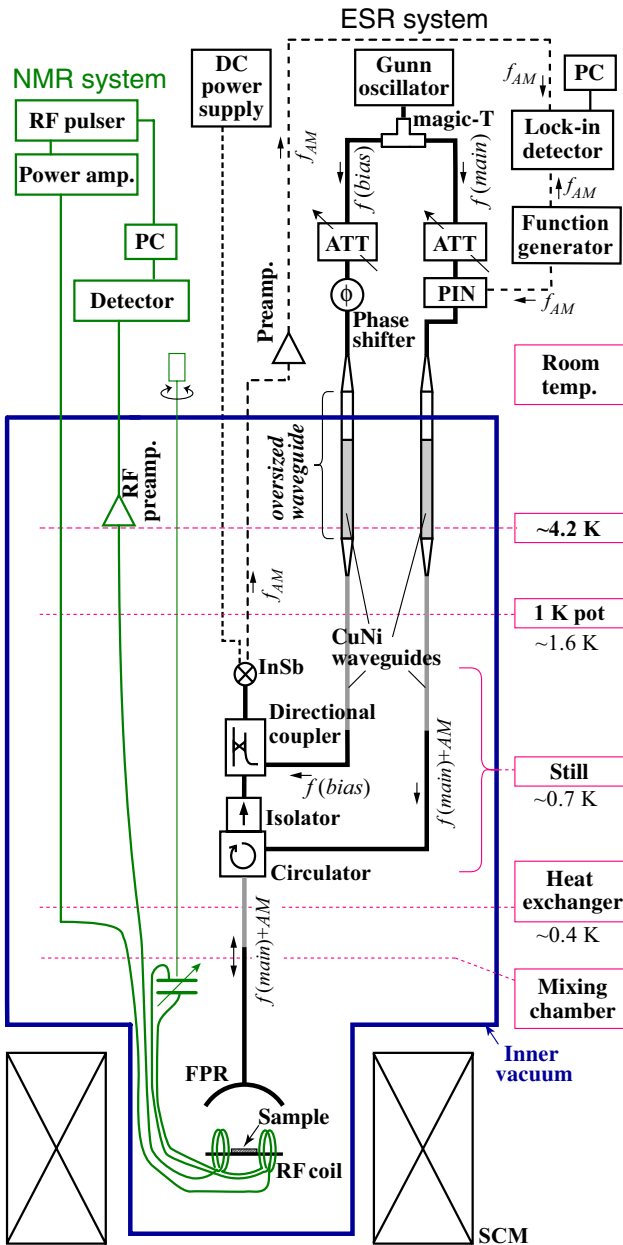
Fig. 1 Schematic of the millimeter-wave ESR system with an FPR in the DR with an SCM. The waveguides made of CuNi are shown in gray. The dashed lines outline the connections by cables. The names of the stages with corresponding temperatures are indicated at the right side (in red boxes) in the figure, to show the temperature change between the room temperature and that of the sample. The thick dashed black lines represent the cable connections carrying low frequencies (~kHz) or DC. The NMR system including cable connections, radio-frequency (RF) coils, and variable capacitor is outlined by the green lines (color figure online)

Millimeter waves from the oscillator are split by a magic-T hybrid (or a directional coupler with a 20-dB coupling) into main and bias lines in the homodyne-detection system, as described in Sect. 3. A 0–50-dB attenuator (ATT) is inserted into each line to adjust the incident power. An amplitude modulation (AM) (Hz–kHz) is applied to the millimeter wave on the main line through a PIN diode. The temperature is measured with ruthenium oxide (RuO) thermometers. To measure the sample temperature, a RuO thermometer is attached to a flat mirror of FPR directly or to the FPR body anchored to the flat mirror. As the output power of the millimeter wave from the Gunn diode is reduced during its traveling through the components by approximately 10 dB before the DR and 20–24 dB inside the DR, the amount of heat produced by the electromagnetic-wave irradiation of the sample area is at most a few tens of microwatts, well below the cooling power of the DR at 0.1 K.

An NMR excitation and detection system, which consists of a conventional pulsed NMR system (THAMWAY Co., Ltd.) with an LC tuning circuit, is attached to the ESR system, as shown in Fig. 1. A preamplifier (N141-206AA, THAMWAY Co., Ltd.) operating at 4 K is utilized. We used coaxial cables made of CuNi and NbTi. The latter one is used to reduce the thermal conductivity between the M/C and 1-K pot stages.

3 FPR

3.1 Design and Variations of the FPR

As discussed above, an FPR is used in our system. The resonator frequency can be adjusted by changing the distance between the two mirrors d [41]. The incident millimeter waves pass through the iris (coupling hole) and reflect between the mirrors, forming TEM_{00q} resonant modes, where q is an integer.

We have developed several types of FPRs. Figure 2 shows the variations of our FPRs. The basic design of the FPR is shown in Fig. 2a, where the two mirrors are made of oxygen-free copper. If the distance d between the mirrors is fixed by, for example, copper blocks, the resonant frequency will depend on the temperature owing to the thermal shrink. Moreover, the sensitivity usually depends on the frequency mainly owing to the impedance transformation between both ends of the waveguide. It is sometimes challenging to find a resonant mode after cooling the FPR, or perform a measurement with an optimal sensitivity. Therefore, it is desirable to adjust the resonant frequency of the FPR even at low temperatures. Such adjustment can be achieved by introducing a home-made piezo actuator on the bottom side, as shown in Fig. 2b. The piezo actuator consists of a piezo stack (PSt 150/7×7/7, Piezo Mechanic Co., Ltd.) glued with a graphite rod. The graphite rod is sandwiched by two blocks made of titanium. When a saw-tooth voltage wave is applied to the piezo stack by a piezo controller (ANC150, Attocube systems AG) through a driver to amplify the voltage (M26110, Mess-Tek Co., Ltd.), the piezo stack expands and contracts repeatedly according to the voltage, and the graphite rod moves up/down by the slip–stick principle. Therefore, the position of the flat mirror
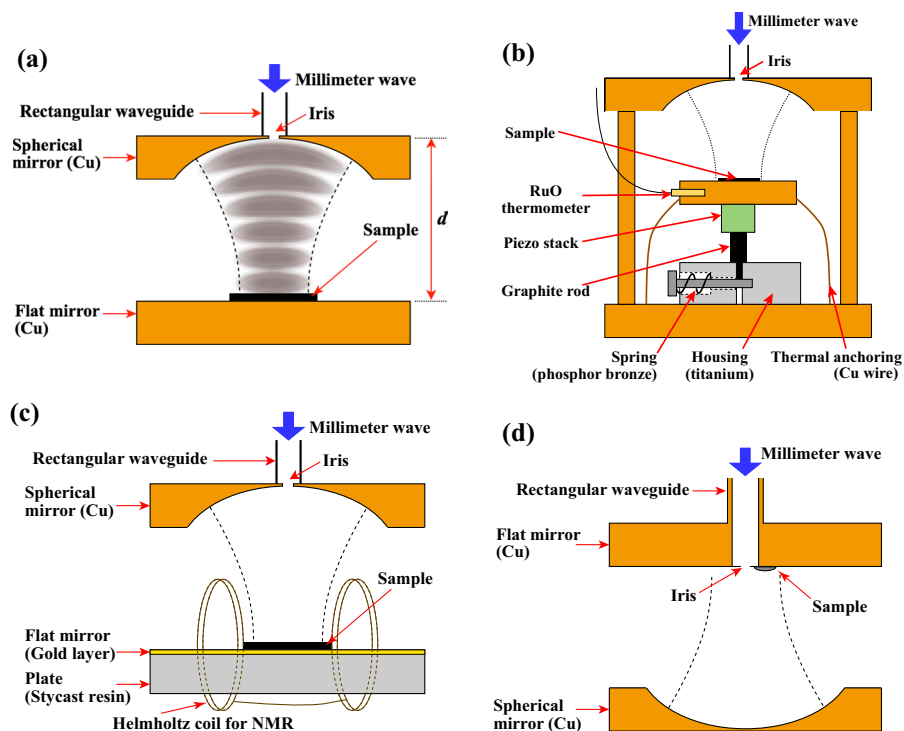
Fig. 2 Cross sections of the FPRs. **a** Basic FPR with spherical and flat mirrors made of copper. **b** Piezo actuator is installed to adjust the mirror distance *d*. **c** FPR for DoMR, whose flat mirror is fabricated using a gold thin film. **d** Flat–spherical FPR

is changed mechanically. The piezo actuator has operated in the temperature from room temperature down to 2.6 K [36]. One may start to move the piezo actuator in a DR at even below 1 K, but the temperature will immediately rise to a few Kelvin or higher.

3.2 FPR with a Gold thin Layer for DoMR

As we aim to perform DoMR, we need a resonator for both ESR and NMR. The FPR is advantageous, over the conventional cylindrical cavities, as the area between the mirrors is open towards the outside. However, the RF field for NMR is disturbed owing to the existence of the copper plate on the sample. To overcome this problem, we utilized the frequency dependence of the skin depth. An RF wave for NMR can transmit through a thin metal layer, while a millimeter wave for ESR is reflected by it. Feher [42] used, for ENDOR experiments at a low field, a rectangular microwave cavity made of silver layer with slits allowing nuclear frequency penetrating into the cavity. This idea is applied to our millimeter-wave FPR, though slits are probably not necessary in our case because of the open structure of the FPR. Figure 2c shows a schematic of a cross section of an FPR with RF coils.

For a compatibility of ESR and NMR, millimeter waves have to be reflected, and RF waves should be transmitted as much as possible. We need to find the suitable film thickness for this requirement. The skin depth can be calculated as follows [43]:

$$\text{skin depth} = \sqrt{2/\omega\mu\sigma}, \tag{1}$$

where $\omega = 2\pi f$ is the angular frequency, f is the operational frequency of the ESR and NMR, μ is the magnetic permeability of the material ($\mu_{\text{gold}} = 4\pi \times 10^{-7}$ H/m), and σ is the electrical conductivity ($\sigma_{\text{gold}} = 4.1 \times 10^7$ S/m at room temperature) [44]. The frequencies used for the example calculations are 128 GHz for ESR and 138 MHz for ^{31}P NMR in Si:P under the same magnetic field. Equation (1) reveals that the target range of the film thickness is 0.22–6.7 μm.

The manufacturing process for a flat gold thin-film mirror is shown in Fig. 3a. First, an epoxy (Stycast 1266) was shaped into a disk (diameter: approximately 30 mm; thickness: approximately 5 mm). The mirror was then polished; after the polishing, the surface roughness was evaluated with a digital microscope (VHX-500F, Keyence Co., Ltd). A thin gold film was then deposited onto the epoxy disk using a coater (SC-701Mk II Advance, Sanyu Electron Co., Ltd).
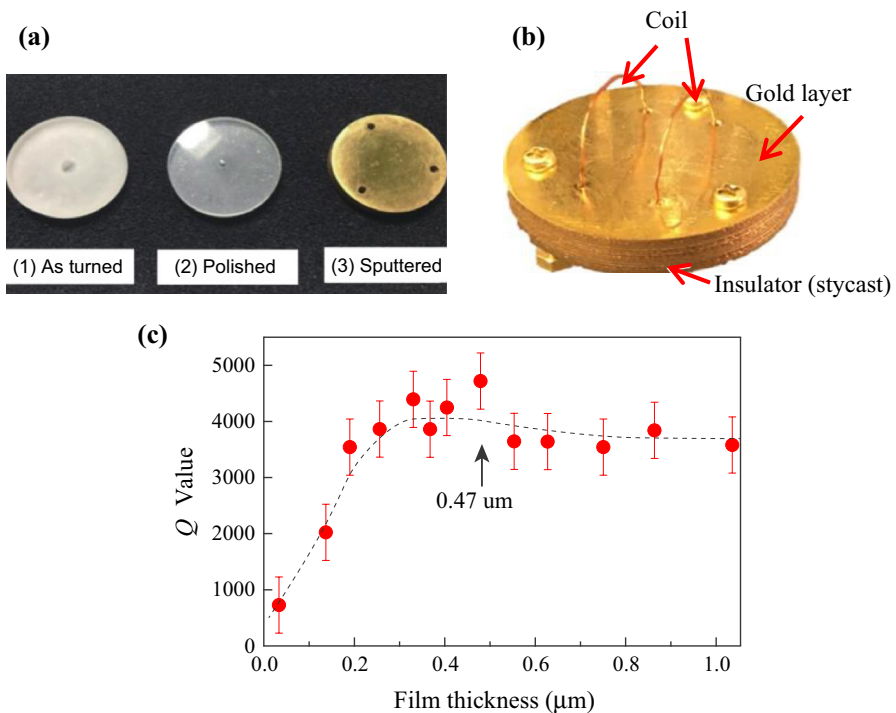

Fig. 3 **a** Photograph showing the development of the flat mirror with a gold film: (1) an as-shaped epoxy resin (Stycast 1266) plate; (2) after polishing with a surface roughness smaller than 8 μm; (3) after deposition of the gold layer by sputtering. **b** Photograph of the flat mirror, coated by the gold layer, with an RF coil. **c** Q value as a function of the thickness of the gold film

The film thickness was determined by fluorescent X-ray measurements (XDV-μ-SDO Fischer scope X-ray System, FISCHER Instruments K.K.). After the calibration using a standard sample with a known film thickness, the fluorescent X-ray intensity was measured on the flat gold thin-film mirror for an X-ray irradiation period of 19 s.

The high Q value of the resonator is an important factor that determines the sensitivity of the ESR measurements. Frequency sweep measurements were performed using a millimeter vector network analyzer (MVNA, Model MVNA8-350-2, AB millimeter). Figure 3c shows the Q values obtained for the FPR with a gold film mirror as a function of the film thickness. The Q value exhibited a maximum or saturated at approximately 0.4–0.5 μm. A minimization of the film thickness is the easiest approach to minimize the disturbance on the RF field by the layer. Therefore, we chose a film thickness of 0.47 μm for the gold film on our flat mirror. The observed surface roughness of the disk was 18 μm (maximum) for a hand-polished disk, which was reduced below 8 μm for a machine-polished disk. The Q value did not significantly depend on the roughness, in the range smaller than 18 μm.

3.3 Flat–Spherical FPR

An FPR (Fig. 2d) with oppositely oriented spherical and flat mirrors was developed, referred to as a flat–spherical FPR. This design is advantageous as the sample on the flat mirror does not move during the adjustment of the resonant frequency, which is very useful for multi-frequency ESR measurements in a wide-frequency range. As the mirror distance has to be changed possibly by a few millimeters, the field inhomogeneity in the sample changes, leading to changes in the lineshape and linewidth. The evaluation of the applied field becomes less accurate. We evaluated the multi-frequency ESR measurements with a regular (spherical–flat) FPR and flat–spherical FPR at 150 K with a ^{4}He-gas flow cryostat. The linewidth significantly changed for the regular FPR, while it was almost constant for the flat–spherical FPR [45]. The results will be reported in another paper.

It is worth noting that the iris of the flat–spherical FPR requires a rather sensitive tuning as the intensity of the electromagnetic wave at the iris is stronger than that of the regular FPR. We have measured Q values and reflection coefficient by changing the diameter of the circular iris with a spherical mirror with a curvature radius of 12.5 mm. The hole with a diameter of approximately 0.56 mm provides a critical coupling independently of the resonant modes.

4 Homodyne Detection

As shown in the previous sections, a homodyne-detection system is constructed in our DR. Compared to the direct transmission or reflection measurements without homodyne or heterodyne detections, the homodyne detection [36–40] has advantages: (1) the sensitivity is better, and (2) absorption and dispersion curves can be obtained selectively. The main disadvantage is the rather narrow-frequency range;

the frequency range in the direct measurement method is basically unlimited except for the cutoff of the waveguide. It is worth noting that a heterodyne detection system [19, 46] provides a higher sensitivity than the homodyne system, though the available frequency range becomes significantly narrower. We present below our homodyne-detection system including measurement results confirming its performance.

In our system, the main-line millimeter wave is guided to the resonator and comes back to InSb after mixing with the bias-line millimeter wave using a directional coupler. An InSb bolometer is used as a detector of the millimeter wave. The AM frequency component of the signal from InSb is obtained by the lock-in detection. The resistance of the InSb detector is approximately proportional to the incident power. Therefore, the change of the voltage detected at InSb, V_{InSb}, is expressed as follows:

$$V_{\text{InSb}} \propto \left(V_{\text{Bias}} + V_{\text{Main}} \right)^2 = V_{\text{Bias}}^2 + V_{\text{Main}}^2 + 2V_{\text{Bias}} V_{\text{Main}} \cos \Delta\varphi, \qquad (2)$$

where V_{Main} and V_{Bias} are the voltages of the main- and bias-line millimeter waves, respectively, and $\Delta\varphi$ is the phase difference between the main- and bias-line millimeter waves, which is controlled by the phase shifter inserted in the bias line. The waveform of V_{Main} may contain an ESR signal. When the effect of the ESR on the cavity resonance is sufficiently small, the reflection coefficient Γ changes its magnitude according to the absorption resonance line; it changes its phase according to the dispersion line. Therefore, the absorption and dispersion lines can be observed selectively by adjusting $\Delta\varphi$ using the phase shifter. Usually, V_{Main} is significantly smaller than V_{Bias}; V_{Main}^2 is negligible, and the ESR signal from V_{Main} is amplified by the application of V_{Bias} owing to the third term of Eq. (2).

Furthermore, two experiments are presented to evaluate our homodyne-detection system. Figure 4 shows the lock-in detected amplitude as a function of the main-line attenuator (main ATT). In these measurements, we used a directional coupler with a 20-dB coupling factor instead of the magic-T hybrid to divide the millimeter-wave output from the Gunn oscillator; the coupled port was connected to the main line. The phase is adjusted to obtain the maximum value of the
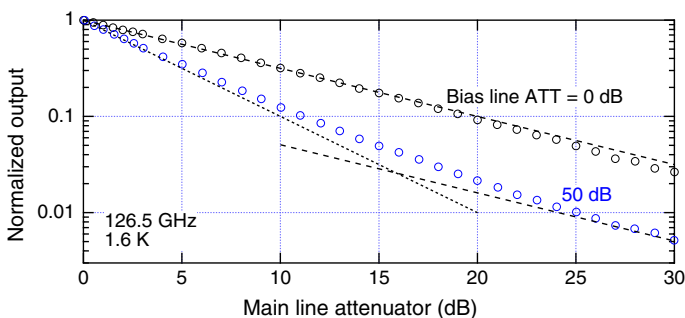

Fig. 4 Dependence of the amplitude of the lock-in detector output on the value of the main-line attenuator measured at the operational frequency of 126.5 GHz, at 1.6 K. The output amplitude is normalized at 0 dB of the main attenuator. The dashed and dotted lines are shown as visual guides to outline the dependences for the second and third terms of Eq. (2), respectively

lock-in output amplitude, which implies that $\Delta\varphi$ is almost zero or π. As shown in the figure, for a sufficiently large V_{Bias} (bias ATT $= 0$ dB), V_{InSb} is proportional to the *voltage* of the main-line millimeter wave, showing the dominance of the third term of the right-hand side of Eq. (2). For a small V_{Bias} (bias ATT $= 0$ dB), V_{InSb} is proportional to the *power* of the main-line millimeter wave for small values of the main ATT, as the second term becomes significant. For the crossover point at a main ATT of approximately 15 dB, $V_{Main} \approx V_{Bias}$. These results are consistent with Eq. (2).

The second evaluation experiment was performed by acquiring ESR spectra from a small amount of DPPH. In this experiment, we used an FPR made of copper. Figure 5 shows the observed ESR spectra using our ESR system with the DR for both absorption and dispersion. The calculated spectra are also shown for comparison. The procedure of the calculation is explained in Appendix A. For the calculation, a Lorentzian-type ESR lineshape is assumed. The half-width of the lineshape at half maximum $1/T_2$ is set to approximately 10^{-9} s^{-1} including the effect of inhomogeneity of the applied field in the sample. The frequency
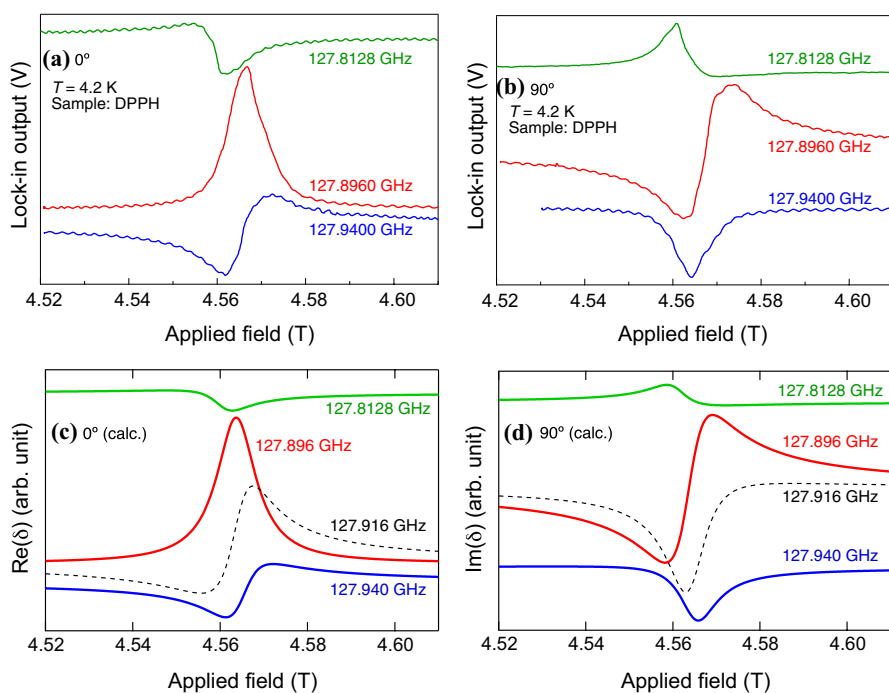

Fig. 5 ESR spectra obtained from the organic radical compound 1,1-diphenyl-2-picrylhydrazyl (it contains 10–20% benzene) (Tokyo Chemical Industry Co., Ltd.), referred to as DPPH for **a** absorption ($\Delta\varphi = 0°$) and **b** dispersion ($\Delta\varphi = 90°$) conditions for three frequencies. The lower panels show calculated spectra for **c** absorption and **d** dispersion conditions for the same frequencies by setting the central resonant frequency of the FPR to 127.8960 GHz. A calculated curve for a frequency deviated by +20 MHz from the central frequency is also shown by the dashed line, to illustrate how rapidly changes the shape of the ESR spectrum with a small deviation from the central frequency

dependence of the spectrum is well reproduced by setting the loaded quality factor Q_L of the resonator to 2×10^3. Therefore, it is confirmed that the homodyne-detection system works properly.

5 ESR Measurements

5.1 ESR Measurements of DPPH

We present the ESR results over the temperature range of 6.5–0.09 K. The sample was a small amount of DPPH powder. As shown in Fig. 6a, the spectra clearly changed over this temperature range. The changes in peak-to-peak (P–P) width are complex, as shown in Fig. 6b. As the temperature decreased below 3.5 K, the P–P width gradually increased, and the intensity decreased. Below approximately 0.5 K, the P–P width again decreased. We also measured the magnetic susceptibility χ of a 6.7-mg DPPH-powder sample in an applied magnetic field of 100 Oe using a superconducting quantum interference device (SQUID) magnetometer (MPMS, Quantum Design) in the temperature range of 2–100 K; the results are shown in Fig. 6c. The susceptibility deviated from the high-temperature Curie–Weiss-type behavior below approximately 20 K, suggesting a development of a short-range antiferromagnetic ordering. A small anomaly in the susceptibility around 6 K was observed, which could be attributed to a small change of the ESR intensity from
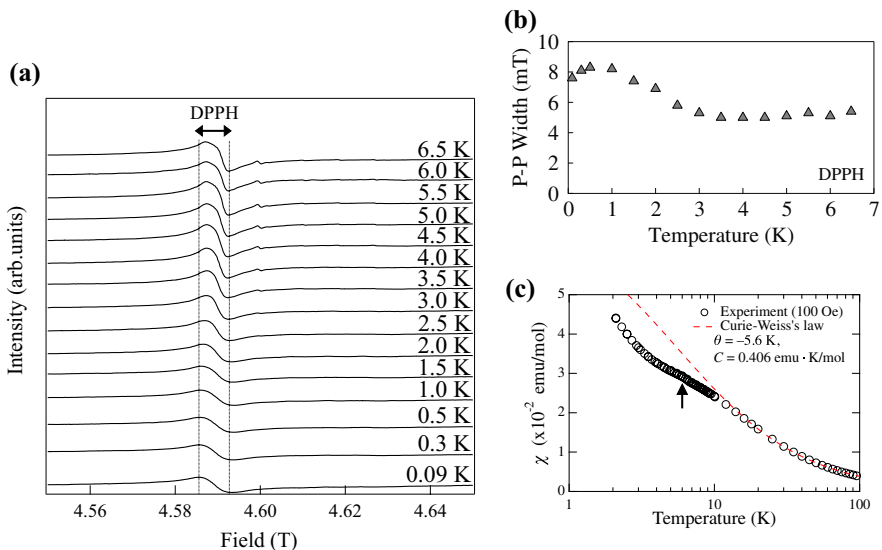

Fig. 6 **a** Dispersion of the ESR signals from DPPH between 6.5 K and 0.09 K. Signals from the $Mn_xMg_{1-x}O$ sample in the FPR are also observed. **b** Temperature dependence of the peak-to-peak width of the ESR spectra of DPPH. **c** Temperature dependence of the magnetic susceptibility of DPPH. The arrow indicates an anomaly around 6 K. The red dashed line represents the Curie–Weiss's law $\chi = C/(T-\theta)$ (color figure online)

DPPH at 6 K, as shown in Fig. 6b, though its origin is still unclear. Considering that the low-temperature behavior of the ESR spectrum, related with the development of magnetic correlations in this material, differs depending on the type of the solvent [47–52], it is important to analyze the crystal structure of our DPPH sample, which has already been measured. Nevertheless, the observed ESR spectrum of the DPPH sample shows almost no shift in the resonance position over the temperature range of 6.5–0.09 K, although the P–P width increases by a factor of approximately 1.5. Therefore, the DPPH sample can be considered a useful standard sample with a magnetic-field accuracy of a few tens of gauss over this temperature range.

5.2 Simultaneous Measurements of ESR and NMR

Before performing DoMR, we have to achieve ESR and NMR measurements with a single FPR. For a ^{31}P-DNP–NMR measurement of Si:P, it is necessary to realize a DNP-enhanced polarization of the nuclear spin system in Si:P owing to the DNP effect.

We discuss the results of ESR and NMR performed at very low temperatures with the DR using an FPR with a flat gold thin-film mirror. We used Si:P ($10\times17\times0.26$ mm^3, ^{31}P concentration: 7.05×10^{16} cm^{-3}, which is in the insulator region [53]) as the sample for ESR measurements. Figure 7 shows an example of an ESR spectrum for Si:P, obtained at 0.25 K and 128.2 GHz. We observed the well-known two-line structure split by the hyperfine interaction [32, 33, 35, 37, 54] as well as a cluster line in-between. The left (low field) and right (high field) lines correspond to the ^{31}P nuclear spin states, "up" and "down", respectively. Therefore, the intensity ratio of the two lines indicates the nuclear spin polarization. As shown in Fig. 7, the nuclear polarization was enhanced owing to the DNP effect after the
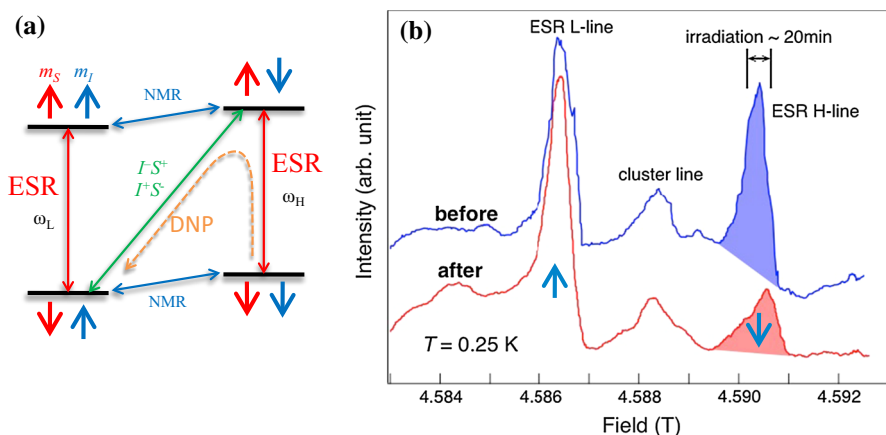

Fig. 7 **a** Four-level energy diagram for Si:P. The dashed line indicates a transition pass producing DNP. **b** ESR spectra of Si:P at 128.2 GHz and 0.25 K obtained before (blue) and after (red) the irradiation of the millimeter wave for 20 min around the H-line. The arrow in each resonance line indicates the corresponding nuclear spin state. The nuclear polarization owing to the DNP effect is observed (color figure online)

Fig. 8 Fourier-transformed
^{1}H-NMR spin-echo signal of
epoxy at 1.3 K using an RF
coil installed on the flat gold
thin-film mirror. The operating
frequency is 26.87 MHz; the
applied field is 0.63 T

FFT ^{1}H-NMR
26.87 MHz
1.3 K

Intensity [arb.units]

Frequency [MHz]
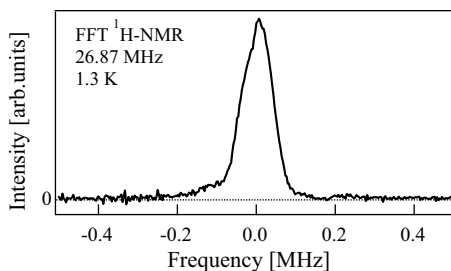
irradiation of the millimeter wave around the right line for 20 min. The obtained nuclear polarization was approximately 50%, hundreds of times larger than the thermal equilibrium polarization. It is confirmed that the flat gold thin-film mirror is efficient as an ESR resonator below 1 K.

As a test of NMR measurements with the FPR, we measured the NMR signal of a proton (^{1}H) contained in the epoxy plate of the flat mirror. Figure 8 shows a Fourier-transformed ^{1}H-NMR signal observed at 1.3 K, under a low field of 0.63 T. This test shows that ESR and NMR measurements can be simultaneously performed using the flat gold thin-film mirror. The filling factor for NMR is very low for these coil shape and configuration. ENDOR measurements could be suitable with this FPR. We are currently developing a new design of the resonator suitable for an NMR detection, which will be reported in a following paper.

6 Summary

We developed a homodyne-detection millimeter-wave ESR measurement system at the University of Fukui using a ^{3}He/^{4}He DR to reach temperatures below 1 K with an operating frequency range of 125–130 GHz. An NMR measurement system was also constructed in this system for an expansion to millimeter-wave ESR/NMR DoMR experiments. The experimental results verified the expected performance of the homodyne-detection system. Several types of FPRs for this system, consisting of spherical and flat mirrors, were developed. The FPR with a piezo actuator enabled to tune the resonance frequency electrically even at low temperatures. The FPR with a coupling iris on a flat mirror was utilized to keep the sample at the same position during the tuning of the resonance frequency. The FPR with a flat mirror fabricated using a gold thin film was developed aiming for DoMR.

ESR and NMR experiments using the FPRs were presented. We performed ESR measurements of a DPPH (it contains 10–20% benzene) powder sample in the temperature range of 6.5–0.09 K. The results suggested that the DPPH sample can be a useful standard sample with a magnetic-field accuracy of a few tens of gauss over this temperature range. In addition, we presented the ESR spectrum from the donor electron spin in Si:P showing the DNP-enhanced nuclear polarization. The NMR signal from ^{1}H contained in the resonator was also detected successfully as well as the ESR signal from Si:P with a single FPR.

Appendix A: ESR Lineshape for the Homodyne System

The calculation procedure for the magnetic-resonance lineshape discussed in Sect. 4 is presented below.

A resonant cavity is often expressed in terms of the microwave analog of a series RLC-tuned circuit [2]. Figure 9 shows an equivalent circuit. The resonant angular frequency ω_0 and unloaded quality factor Q_0 are expressed as follows:
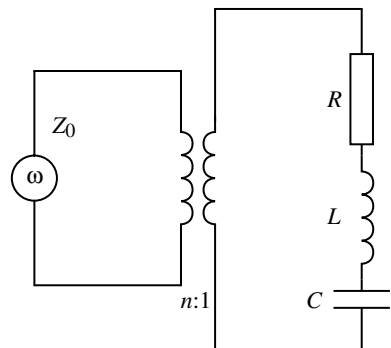
$$\omega_0 = \frac{1}{\sqrt{LC}}, \tag{3}$$

$$Q_0 = \frac{1}{R}\sqrt{\frac{L}{C}}, \tag{4}$$

where R, L, and C are the resistance, inductance, and capacitance, respectively. The impedance of the circuit is as follows:

$$Z = R + i\left(\omega L - \frac{1}{\omega C}\right). \tag{5}$$

Fig. 9 LCR circuit equivalent to the FPR coupled with the oscillator through a waveguide

For a reflection cavity, such as our FPR, a waveguide with an impedance Z_0 is coupled to the cavity with a coupling coefficient (or coupling parameter) β:

$$\beta = \frac{Z_0}{n^2 R}. \tag{6}$$

The impedance from the waveguide Z_L is:

$$Z_L = n^2 Z. \tag{7}$$

We measure the loaded quality factor Q_L from the waveguide:

$$Q_L = \frac{Q_0}{1 + \beta}. \tag{8}$$

If the cavity is perfectly coupled or matched to the waveguide, then $\beta = 1$ and $Q_L = Q_0/2$..

Furthermore, we consider the case when the cavity contains a magnetic sample with a magnetic susceptibility $\chi = \chi' - i\chi''$. The effect of the electric permeability is assumed to be negligible. The parameters L, R, Z, and β are expressed as follows:

$$L^* = L(1 + q\chi'), \tag{9}$$

$$R^* = R + q\omega L\chi'' = R\left(1 + qQ_0\frac{\omega}{\omega_0}\chi''\right), \tag{10}$$

$$Z^* = R^* + i\left(\omega L^* - \frac{1}{\omega C}\right), \tag{11}$$

$$\beta^* = \frac{Z_0}{n^2 R^*}, \tag{12}$$

where q is the filling factor of the sample. The reflection coefficient without the sample $\Gamma(\omega)$ is:

$$\Gamma(\omega) = \frac{Z_L - Z_0}{Z_L + Z_0} = \frac{1 - \beta + iQ_0\left(\frac{\omega}{\omega_0} - \frac{\omega_0}{\omega}\right)}{1 + \beta + iQ_0\left(\frac{\omega}{\omega_0} - \frac{\omega_0}{\omega}\right)}. \tag{13}$$

The reflection coefficient with the sample $\Gamma^*(\omega)$ is obtained in the same manner:

$$\Gamma^*(\omega) = \frac{1 - \beta^* + iQ_0^*\left(\frac{\omega}{\omega_0^*} - \frac{\omega_0^*}{\omega}\right)}{1 + \beta^* + iQ_0^*\left(\frac{\omega}{\omega_0^*} - \frac{\omega_0^*}{\omega}\right)}, \tag{14}$$

where,

$$\omega_0^* = \frac{\omega_0}{\sqrt{1 + q\chi'}}, \tag{15}$$

$$Q_0^* = Q_0 \frac{\sqrt{1 + q\chi'}}{1 + qQ_0 \frac{\omega}{\omega_0} \chi''}, \tag{16}$$

$$\beta^* = \frac{\beta}{1 + qQ_0 \frac{\omega}{\omega_0} \chi''}. \tag{17}$$

We can rewrite Eq. (14) as:

$$\Gamma^*(\omega) = \frac{1 - \beta + qQ_0 \frac{\omega}{\omega_0} \chi'' + iQ_0 \left(\frac{\omega}{\omega_0} \left(1 + q\chi' \right) - \frac{\omega_0}{\omega} \right)}{1 + \beta + qQ_0 \frac{\omega}{\omega_0} \chi'' + iQ_0 \left(\frac{\omega}{\omega_0} (1 + q\chi') - \frac{\omega_0}{\omega} \right)}. \tag{18}$$

We define the reflection coefficient for an empty cavity at $\omega = \omega_0$ as:

$$\Gamma_0 = \frac{1 - \beta}{1 + \beta}, \tag{19}$$

and define $\gamma = qQ_L\chi$ ($\gamma' = qQ_L\chi'$, $\gamma'' = qQ_L\chi''$); we obtain:

$$\Gamma^*(\omega) = \frac{\Gamma_0 + \gamma'' \frac{\omega}{\omega_0} + iQ_L \left(\frac{\omega}{\omega_0} - \frac{\omega_0}{\omega} \right) + i \left(\frac{\omega}{\omega_0} \right) \gamma'}{1 + \gamma'' \frac{\omega}{\omega_0} + iQ_L \left(\frac{\omega}{\omega_0} - \frac{\omega_0}{\omega} \right) + i \left(\frac{\omega}{\omega_0} \right) \gamma'}. \tag{20}$$

For the resonance frequency (ω_0):

$$\Gamma^* = \frac{\Gamma_0 + i\gamma}{1 + i\gamma}. \tag{21}$$

The measured ESR signal is expressed by:

$$\delta = \frac{\Gamma^* - \Gamma_0}{\Gamma_0}. \tag{22}$$

It is well known that $\chi''(\omega)$ and $\chi'(\omega)$ correspond to the absorption and dispersion lines of the magnetic resonance, respectively, related to each other by the Kramers–Kronig relation. Therefore, it is useful to express δ in terms of γ:

$$\delta = \eta \left[\frac{\gamma'' + \gamma''^2 + \gamma'^2 + i\gamma'}{(1 + \gamma'')^2 + \gamma'^2} \right], \tag{23}$$

where:

$$\eta = \frac{2\beta}{1 - \beta} = 1 - \frac{1}{\Gamma_0}. \tag{24}$$

The real and imaginary parts of δ contain both $\chi''(\omega)$ and $\chi'(\omega)$; therefore, the observed ESR signals are not perfectly separated into absorption and dispersion signals. Nevertheless, it is known that the mixing becomes significant when the spin density is approximately larger than 3×10^{15} cm^{-3} [38]. As the spin density is sufficiently small for our measurements, we can observe almost pure dispersion and absorption signals as the real and imaginary parts of δ, respectively.

In the calculation shown in Sect. 4, we used a Lorentzian-like lineshape:

$$\chi'(\omega) = \frac{\chi_0 \gamma_e^2 H_0^2 \left(\gamma_e^2 H_0^2 - \omega^2 \right)}{\left(\gamma_e^2 H_0^2 - \omega^2 \right)^2 + 4\omega^2 / T_2^2}, \tag{25}$$

$$\chi''(\omega) = \frac{2\chi_0 \gamma_e^2 H_0^2 \omega / T_2}{\left(\gamma_e^2 H_0^2 - \omega^2 \right)^2 + 4\omega^2 / T_2^2}, \tag{26}$$

where γ_e is the gyromagnetic ratio of the electron, H_0 is the applied field, and χ_0 is the uniform susceptibility. These equations are derived from the Bloch's equations, without saturation and with a long spin–spin relaxation time T_2 [55]. Slightly different equations are obtained in Refs. [4] and [33], though the obtained lineshape is very close to that corresponding to the above equations. The free parameters for the calculations shown in Fig. 4 are the relaxation rate $1/T_2$ revealing the width of the lineshape, Q_L determining the frequency dependence, and scaling factor including q and χ_0.

References

1. R.S. Alger, *Electron Paramagnetic Resonance: Techniques and Applications*, 2nd edn. (Wiley, New York, 1968)
2. C.P. Poole Jr., *Electron Spin Resonance*, 2nd edn. (Dover Publications Inc., New York, 1983)
3. C.P. Slichter, *Principles of Magnetic Resonance with Example from Solid State Physics* (Harper&Row Publications Inc., New York, 1963)

4. B. Cowan, *Nuclear Magnetic Resonance and Relaxation* (Cambridge University Press, Cambridge, 1997)
5. L. Balents, Nature **464**, 11 (2010)
6. H. Okura, K. Ishida, Y. Kawasaki, Y. Kitaoka, Y. Yamamoto, Y. Miyako, T. Fukuhara, K. Maezawa, Physica. B **281–282**, 61 (2000)
7. Y. Fujii, T. Goto, K. Awaga, T. Okuno, Y. Sasaki, T. Mizusaki, J. Magn. Magn. Mater. **177–181**, 991 (1998)
8. T. Itou, A. Oyamada, S. Maegawa, R. Kato, Nat. Phys. **6**, 673 (2010)
9. M. Jeong, H. Mayaffre, C. Berthier, D. Schmidiger, A. Zheludev, M. Horvatić, Phys. Rev. Lett. **118**, 167206 (2017)
10. A. Koda, W. Higemoto, R. Kadono, K. Ishida, Y. Kitaoka, C. Geibel, F. Steglich, Physica. B **281–282**, 16 (2001)
11. F. Xiao, J.S. Möller, T. Lancaster, R.C. Williams, F.L. Pratt, S.J. Blundell, D. Ceresoli, A.M. Barton, J.L. Manson, Phys. Rev. B **91**, 144417 (2015)
12. R.N. Ruby, H. Benoit, P.L. Scott, C.D. Jeferies, Bull. Am. Phys. Soc. Series II **6**, 512 (1962)
13. V.B. Fedorov, Cryogenics **5**, 911 (1965)
14. K. Oshima, K. Okuda, M. Date, J. Phys. Soc. Jpn. **41**, 475 (1976)
15. K. Oshima, K. Okuda, M. Date, J. Phys. Soc. Jpn. **44**, 757 (1978)
16. K. Koyama, M. Yoshida, T. Sakon, D.X. Li, T. Suzuki, M. Motokawa, J. Phys. Soc. Jpn. **69**, 3425 (2000)
17. M. Mola, S. Hill, P. Goy, M. Gross, Rev. Sci. Instrum. **71**, 186 (2000)
18. T. Sakon, H. Nojiri, K. Koyama, T. Asano, Y. Ajiro, M. Motokawa, J. Phys. Soc. Jpn. **72**, 140 (2003)
19. S.A. Vasiliyev, J. Järvinen, E. Tjukanoff, A. Kharitonov, S. Jaakkola, Rev. Sci. Instrum. **75**, 94 (2004)
20. M. Hagiwara, T. Kashiwagi, H. Yashiro, T. Umeno, T. Ito, T. Sano, J. Phys: Conf. Ser. **150**, 012015 (2009)
21. S. Sheludiakov, J. Ahokas, O. Vainio, J. Järvinen, D. Zvezdov, S. Vasiliev, V.V. Khmelenko, S. Mao, D.M. Lee, Rev. Sci. Instrum. **85**, 053902 (2014)
22. J. Järvinen, J. Ahokas, S. Sheludyakov, O. Vainio, L. Lehtonen, S. Vasiliev, D. Zvezdov, Y. Fujii, S. Mitsudo, T. Mizusaki, M. Gwak, S.-G. Lee, S. Lee, L. Vlasenko, Phys. Rev. B **90**, 214401 (2014)
23. C.A. McDowell, A. Naito, J. Magn. Reson. **45**, 205 (1981)
24. C.A. McDowell, A. Naito, D.L. Sastry, Y.U. Cui, K. Sha, S.X. Yu, J. Mol. Struct. **195**, 361 (1989)
25. B. Epel, A. Pöppl, P. Manikandan, S. Vega, D. Goldfarb, J. Magn. Reson. **148**, 388 (2001)
26. G.W. Morley, L.C. Brunel, J.V. Tol, Rev. Sci. Instrum. **79**, 064703 (2008)
27. J.H. Ardenkjæ-Larsen, B. Fridlund, A. Gram, G. Hansson, L. Hansson, M.H. Lerche, R. Servin, M. Thaning, K. Golman, Proc. Natl. Acad. Sci. USA **100**, 18 (2003)
28. K.R. Thurber, W.M. Yau, R. Tycko, J. Magn. Reson. **204**, 303 (2010)
29. J. Leggett, R. Hunter, J. Granwehr, R. Panek, A.J. Perez-Linde, A.J. Horsewill, J. McMaster, G. Smith, W. Köckenberger, Phys. Chem. Chem. Phys. **12**, 5883 (2010)
30. Y. Matsuki, H. Takahashi, K. Ueda, T. Idehara, I. Ogawa, M. Toda, H. Akutsu, T. Fujiwara, Phys. Chem. Chem. Phys. **12**, 5799 (2010)
31. L. Lumata, M. Merritt, C. Khemtong, S.J. Ratnakar, V.J. Tol, L. Yu, L. Song, Z. Kovacs, RSC Adv. **2**, 12812 (2012)
32. A.W. Overhauser, Phys. Rev. **92**, 411 (1953)
33. A. Abragam, *The Principles of Nuclear Magnetism* (Clarendon Press, Oxford, 1961)
34. B.E. Kane, Nature **393**, 133 (1998)
35. Y. Fujii, S. Mitsudo, K. Morimoto, T. Mizusaki, M. Gwak, S.G. Lee, A. Fukuda, A. Matsubara, T. Ueno, S. Lee, J. Phys: Conf. Ser. **568**, 042005 (2014)
36. Y. Ishikawa, K. Ohya, Y. Fujii, Y. Koizumi, S. Miura, S. Mistudo, A. Fukuda, T. Asano, T. Mizusaki, A. Matsubara, H. Kikuchi, H. Yamamori, J. Infra. Millim. THz Waves **39**, 288 (2018)
37. Y. Ishikawa, K. Ohya, Y. Fujii, A. Fukuda, S. Miura, S. Mitsudo, H. Yamamori, H. Kikuchi, J. Infra. Millim. THz Waves **39**, 387 (2018)
38. S.A. Vasilyev, A.Ya. Katunin, A.I. Safonov, A.V. Frolov, E. Tjukanov, Appl. Magn. Reson. **3**, 1061 (1992)
39. A. Fukuda, H. Takenaka, T. Mizusaki, J. Low Temp. Phys. **121**, 737 (2000)
40. A. Fukuda, H. Takenaka, T. Ohmi, T. Mizusaki, J. Low Temp. Phys. **126**, 127 (2001)
41. H. Kogelnik, T. Li, Proc. IEEE **54**, 10 (1966)
42. G. Feher, Phys. Rev. **114**, 1219 (1959)

43. S. Gonda, *Preparation and Evaluation of Thin Film and Application Technique Handbook (in Japanese)* (Fuji-Technosystem Co., Ltd., Tokyo, 1984)
44. R.A. Serway, Principles of Physics, 2nd edn., (Saunders College Pub, Fort Worth. 1998), p. 602 **(ISBN: 0-03-020457-7)**
45. S. Miura, K. Ohya, Y. Ishikawa, Y. Fujii, H. Kikuchi, A. Fukuda, S.Mitsudo, M. Toda, in *Abstracts of the 56th Annual Meetings of the Society of Electron Spin Science and Technology (SEST2017)* (Tokyo, Japan, 2-4 November 2017) Paper PS67
46. B.W. Statt, W.N. Hardy, A.J. Berlinsky, E. Klein, J. Low Temp. Phys. **61**, 471 (1985)
47. A.M. Prokhorov, V.B. Fedorov, Soviet Phys. JETP **16**, 1489 (1963)
48. T. Fujito, Bull. Chem. Soc. Jpn. **54**, 3110 (1981)
49. J. Krzystek, A. Sienkiewicz, L. Pardi, L.C. Brunel, J. Magn. Reson. **125**, 207 (1997)
50. D. Žilić, D. Pajić, M. Jurić, K. Molčanov, B. Rakvin, P. Planinić, K. Zadro, J. Magn. Reson. **207**, 34 (2010)
51. W. Voesch, M. Thiemann, D. Bothner, M. Dressel, M. Scheffler, Phys. Procedia **75**, 503 (2015)
52. G.B. Teitel'baum, E.G. Kharakhash'yan, S.Ya. Khlebnikov, A.G. Zenin, JETP Lett. **34**, 555 (1981)
53. T.F. Rosenbaum, R.F. Milligan, M.A. Paalanen, G.A. Thomas, R.N. Bhatt, W. Lin, Phys. Rev. B **27**, 7509 (1983)
54. G. Feher, R.C. Fletcher, E.A. Gere, Phys. Rev. **100**, 1784 (1955)
55. M. Date, *Electron Spin Resonance (in Japanese)* (Baifukan, Tokyo, 1978)